X-ray standing wave technique with spatial resolution: In-plane characterization of surfaces and interfaces by full-field x-ray fluorescence imaging

Wenyang Zhao and Kenji Sakurai*
University of Tsukuba, 1-1-1, Tennodai, Tsukuba, Ibaraki 305-0006, Japan
and National Institute for Materials Science, 1-2-1, Sengen, Tsukuba, Ibaraki 305-0047, Japan

(Received 26 June 2018; revised manuscript received 22 November 2018; published 12 February 2019)

The present paper describes a powerful extension of the x-ray standing-wave technique that combines it with the capability of full-field x-ray fluorescence imaging, so that the impurity depth profiles at all different parts of a nanolayer material can be measured in parallel. The imaging capability improves the robustness and reliability of the x-ray standing-wave technique in investigating inhomogeneous two-dimensional materials and soft interfaces. It can also visualize the three-dimensional element-specific structure at a buried interface with a depth resolution at the nanometer level.

DOI: 10.1103/PhysRevMaterials.3.023802

I. INTRODUCTION

The x-ray standing-wave (XSW) field [1] created by the interference of incident x-ray waves and reflected x-ray waves creates an atomic-scale yardstick for measuring the precise position of impurities in their host materials. Theoretically speaking, this works for any material where strong x-ray interference can be induced, e.g., Bragg diffraction in a perfect single crystal, total reflection at a smooth surface, and multiple reflections in a periodic multilayer (PML). In these materials, the XSW field has a periodic intensity variation in the direction normal to the reflection planes. Also, the XSW field moves in the normal direction when the angle between the propagation direction of the incident waves and the reflection waves changes slightly. As the x-ray fluorescence (XRF) intensity of an impurity is proportional to the XSW intensity at its location, one can study the distribution of the impurity in the normal direction by analyzing how its XRF intensity changes during an angle scan. More than 50 years ago, the technique was first presented by Batterman to determine the foreign atom sites in a single crystal [2,3]. Subsequently, the technique was further developed to locate adsorbates at a crystal surface [4,5]; to investigate the impurities in a layered synthetic structure [6,7]; to probe the electrochemical deposition, diffusion layers, and biomembranes at a solid/air or solid/liquid interface [8–11]; and even to sketch the concentration profile of the solute at a liquid/air interface [12]. Today, the technique is widely applied to characterize various nanolayer structures and interfaces.

While the XSW technique has an atomic-scale resolution in the direction perpendicular to the reflection plane, it has no spatial resolution parallel to the reflection plane. On the other hand, in XSW analysis, the probing area is determined by the illumination area of the incident x rays, which is frequently larger than a few square millimeters. Therefore, when the XSW technique is applied to investigating the impurities in materials, the depth distribution of the impurity should be identical for every point in the probing area. However, for some ultrathin nanolayers and interfaces, maintaining in-plane uniformity over such a wide area is difficult. For this reason, it is necessary to combine the existing XSW technique with an in-plane imaging capability. As the area of nanolayers and interfaces is frequently a few square centimeters to square millimeters, an imaging resolution at the submillimeter level to micron level is already sufficient to match the macroscopic in-plane inhomogeneity of the entire sample.

Full-field XRF imaging is an efficient technique for providing the in-plane spatial resolution. This technique utilizes an energy-dispersive x-ray imager as the detector and employs appropriate x-ray optics to project XRF images from the sample to the imager. In recent years, full-field XRF imaging has become increasingly popular. Many new detectors and x-ray optical components have been developed and established [13–17]. In this paper, a complementary metal oxide semiconductor (CMOS) camera was employed as an energy-dispersive XRF imager [18,19] and a micropinhole was inserted between the sample and the camera; thus it is possible to upgrade conventional XSW analysis for XSW imaging technique (Fig. 1). In the scheme of conventional XSW analysis [Fig. 1(a)], the XRF intensity profile $Y(\theta)$ with respect to the angle scan is measured for all the impurity locations combined; thus, the resolved $\rho(z)$ represents the average depth distribution of the impurity throughout the entire probing area. In contrast, in the scheme of XSW imaging [Fig. 1(b)], the in-plane imaging capability splits the entire probing area into many independent pieces; thus, the acquired XRF intensity profile $Y_{x,y}(\theta)$ reveals the impurity depth profile $\rho_{x,y}(z)$ specifically at (x, y). In this way, the XSW imaging technique provides a systematic description of the impurity locations when the impurity depth distribution has in-plane variation in the sample. The application of XSW analysis can be extended to nonuniform nanolayers and interfaces.

In the present paper, the necessity of XSW imaging for a nonuniform sample is demonstrated using analytical expressions. The experimental setup for XSW imaging is

*sakurai@yuhgiri.nims.go.jp

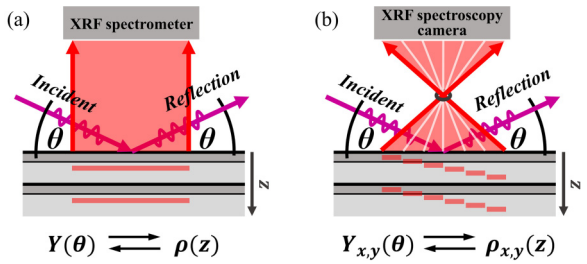

FIG. 1. (a) Conventional XSW analysis. It measures the full-field XRF intensity profile $Y(\theta)$ and analyzes the average depth distribution $\rho(z)$ of the impurity over the entire probing area. (b) XSW imaging technique. It measures $Y_{x,y}(\theta)$ independently at every (x, y) point and reveals their respective impurity depth distribution $\rho_{x,y}(z)$.

constructed and the distribution of the impurity in a PML sample is investigated. All the experimental results are displayed and a method of feature mapping is proposed to process the large amounts of XSW imaging data. Moreover, future optimization of the technique is discussed, and a wide range of promising applications are summarized.

II. EXPERIMENT

In this paper, the sample had a total of 150 nickel/carbon bilayers coated on a 0.25-mm-thick silicon substrate. Based on our previous XRF study, the sample was known to contain a small amount of iron as an impurity. The aim of the experiment was to investigate the distribution of the iron impurity within the periodic multilayers.

The experiment was carried out using a rotating-anode x-ray tube with a copper target (Ultrax 18, Rigaku). The tube power was 40 kV and 300 mA. The x-ray tube was equipped with a 40-mm-long tungsten/silicon x-ray mirror as the monochromator to pass Cu Kα x rays (8047 eV). In addition, 16-μm-thick nickel foils were inserted in the incident beam path to remove the contamination of Cu Kβ x rays. The size of the incident beam was 0.2 mm (H) $\times$ 10 mm (V). It could irradiate a wide area on the sample at glancing incidence. The angular divergence of the incident beam was 0.025°. The intensity arriving at the sample was approximately 8×10^7 counts per second.

The layer structure of the Ni/C PML sample was determined by measuring its x-ray reflectivity (XRR) pattern (RINT-2000, Rigaku). In this measurement, the slit for collimating the incident x-ray beam was temporarily changed to 0.05 mm in width. The angular resolution of the XRR measurement was 0.03°.

The distribution of the iron impurity was investigated by the XSW imaging technique. In the experiment, a full-field XRF imaging setup was placed in front of the sample. The setup consisted of a CMOS camera (pco.edge 5.5) and a micropinhole. Initially the CMOS camera had been designed for taking ordinary photos in visible light. However, after our modification, the camera became able to record the energy of every detected x-ray photon when it worked in single-photon-counting mode [18,19]. The pixel size of the camera is 6.5 $\times$ 6.5 μm, the number of pixels is 2560 $\times$ 2160, and the active area of the sensor is 16.6 $\times$ 14.0 mm. The micropinhole was installed between the sample and the camera sensor. It was drilled in a 25-μm-thick tungsten foil and the pinhole diameter was 200 μm. It was located 4.5 mm from the sample surface and 13.5 mm from the camera sensor. Therefore, the magnification of full-field XRF imaging was factor 3, and consequently the probing area on the sample was 5.5 $\times$ 4.7 mm. In this condition, the spatial resolution of imaging was tested to be 160 μm by measuring a standard resolution target. In the XSW imaging experiment, energy-dispersive XRF images were recorded while the glancing angle between the incident x-ray beam and the sample surface was scanned around the Bragg diffraction angle of the Ni/C PML sample.

In order to compare the XSW imaging technique with the conventional XSW analysis, after the XSW imaging experiment, the full-field XRF imaging setup was replaced by a Si-PIN XRF detector (Amptek, X-123). In this step, XRF spectra were recorded while the glancing angle was scanned again around the Bragg diffraction angle.

III. RESULTS AND DISCUSSION

A. Analytical expressions for XSW imaging for a PML sample

The necessity of XSW imaging for a nonuniform sample was verified using analytical expressions. The derivation starts from a uniform PML sample. In this paper, the Ni/C PML sample was prepared by a repeated coating process; therefore, the depth distribution of the iron impurity is assumed to be identical in every Ni/C bilayer. Imitating the equations for XSW Fourier analysis [20,21], two quantities are employed to describe the depth distribution of the iron impurity in each Ni/C bilayer. The first one is the coherent position, z_A. It describes the "average" position of the impurity in the depth direction. The second one is the coherent fraction, f_A. It relates to the spreading width of the impurity in the depth direction. Then, the XRF intensity of the iron impurity inside the nth Ni/C bilayer of the PML sample is

$$Y_n(\theta) = A_n I_n(\theta)\Big\{1 + R_n(\theta) + 2\sqrt{R_n(\theta)} f_A \times \cos\Big[\nu(\theta) - 2\pi\frac{z_A}{D}\Big]\Big\}, \quad (1)$$

where θ denotes the glancing angle between the incident x-ray beam and the sample surface, A_n denotes the escape ratio of the XRF from the nth bilayer, $I_n(\theta)$ denotes the incident x-ray intensity at the nth bilayer, $R_n(\theta)$ denotes the corresponding reflectivity, $\nu(\theta)$ denotes the phase difference between the reflection x-ray waves and the incident waves at the reference plane in the nth bilayer, and D denotes the thickness of a Ni/C bilayer. Equation (1) is valid when θ is scanned around the Bragg diffraction angle θ_B. In this condition a strong XSW field forms.

In this paper, the PML sample has 150 Ni/C bilayers. Therefore, the total XRF intensity integrated from all 150 bilayers is

$$Y(\theta) = \sum_{n=1}^{150} Y_n(\theta) = P(\theta) + Q(\theta) f_A \cos\Big[\nu(\theta) - 2\pi\frac{z_A}{D}\Big], \quad (2)$$

where

$$P(\theta) = \sum_{n=1}^{150} A_n I_n(\theta)[1 + R_n(\theta)],$$
$$Q(\theta) = \sum_{n=1}^{150} 2A_n I_n(\theta)\sqrt{R_n(\theta)}. \quad (3)$$

In Eq. (2), when θ is scanned across the Bragg diffraction angle θ_B, the phase factor $v(\theta)$ changes by π. Therefore, the XRF intensity profile $Y(\theta)$ around θ_B is distorted from half a period of a cosine function. The two distortion factors $P(\theta)$ and $Q(\theta)$ can be calculated by applying Parratt's recursive equations [22] to the layer structure of the PML sample. The information about the impurity depth distribution is coded in the XRF intensity profile $Y(\theta)$. A detailed discussion of Eqs. (2) and (3) is provided in the Supplemental Material [23].

Until now, it has been assumed that the impurity depth distribution is identical for any point on the sample. In this case, measuring the full-field XRF intensity profile $Y(\theta)$ is sufficient no matter how large the probing area is. However, for a nonuniform sample, the depth distribution of the impurity may vary with respect to the in-plane position (x, y). In this case, the coherent position z_A and the coherent fraction f_A become dependent on (x, y) and they should be denoted by $z_{A_{x,y}}$ and $f_{A_{x,y}}$, respectively. Then, the full-field XRF intensity from the entire probing area is a summation of the intensity components at all (x, y) points, which is

$$\begin{aligned} Y(\theta) &= \sum_x \sum_y Y_{x,y}(\theta) \\ &= P(\theta) + Q(\theta) \sum_x \sum_y C_{x,y} f_{A_{x,y}} \cos\left[v(\theta) - 2\pi \frac{z_{A_{x,y}}}{D}\right] \\ &= P(\theta) + Q(\theta) f_A{}' \cos\left[v(\theta) - 2\pi \frac{z_A{}'}{D}\right]. \end{aligned} \quad (4)$$

Here, $C_{x,y}$ denotes the amount of the impurity at (x, y). In Eq. (4), the summation of all cosine components yields a new phase z_A' and a reduced amplitude f_A'. Thus, by measuring the full-field XRF intensity profile $Y(\theta)$, one only obtains an "average" estimation, which is a compromise based on the impurity depth distribution at all (x, y) points in the entire probing area. In the meantime, the variation of the XRF intensity with respect to the angle scan also becomes less noticeable. Therefore, for a nonuniform sample in which the impurity depth distribution has some in-plane variation, the scheme of conventional XSW analysis may not work, or the analysis may be strongly biased by several abnormal points of high impurity concentration. Consequently, for an unknown sample, it is necessary to measure the XRF intensity profile $Y_{x,y}(\theta)$ at every point independently. This is precisely the aim of the XSW imaging technique presented in this paper.

B. Layer structure of the Ni/C PML sample

The layer structure of the Ni/C PML sample was determined by measuring and fitting its XRR pattern (Fig. 2). In the pattern, the first to the sixth Bragg diffraction peaks are shown. The first diffraction peak is at $\theta_B = 0.93°$. The angle position of the six diffraction peaks indicates the bilayer thickness D, and their intensity ratio indicates the thickness ratio of the nickel layer to the carbon layer in every bilayer, and the interface roughness. The full pattern of XRR fitting was simulated by using Parratt's recursive equations [22]. In order to simulate the interface roughness, a set of thin slices with step-changing refractive indices was inserted at every interface. After that, the simulated XRR pattern was convoluted with a Gaussian function that represents the angular resolution of the XRR measurement. The simulated XRR pattern matched well with the experimental pattern, especially for the position and the intensity of the six Bragg diffraction peaks. It is noted that the high-order Bragg diffraction peaks in the experiment are wider than those in the simulation. This disagreement is due to the influence of diffuse scattering and the deviation of the bilayer thickness D in the 150 repetitions.

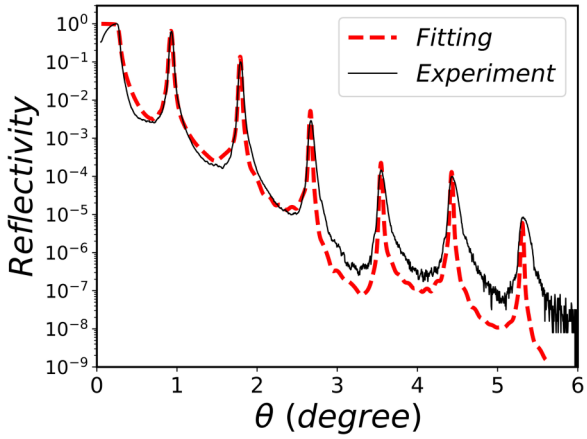

FIG. 2. XRR pattern of the nickel/carbon periodic multilayer.

The layer structure parameters obtained from fitting are listed in Table I.

C. XSW imaging experiment data

Based on the XRR measurement, the first Bragg diffraction peak of the Ni/C PML sample is at $\theta_B = 0.93°$. In the XSW imaging experiment, the glancing angle between the incident x-ray beam and the sample surface was scanned around θ_B. At every angle, energy-dispersive XRF images were measured, and the measurement time was 6 h. Figure 3 shows examples of the experimental data. The full-field XRF spectra were measured over the entire probing area [Fig. 3(a)]. In the spectra, the peaks of iron and chromium correspond to the impurities inside the sample. The peak of Si Kα, β corresponds to the silicon substrate. The major constituents of the sample, nickel and carbon, are not shown in the spectra because nickel K lines were not excited and carbon K lines

TABLE I. The layer structure of the nickel/carbon periodic multilayer.

Feature	Value	Feature	Value
Bilayer thickness D	50 Å	Interface roughness (rms)	6.5 Å
Nickel layer thickness	14 Å	Nickel layer density	8.0 g/cm^3
Carbon layer thickness	36 Å	Carbon layer density	2.1 g/cm^3

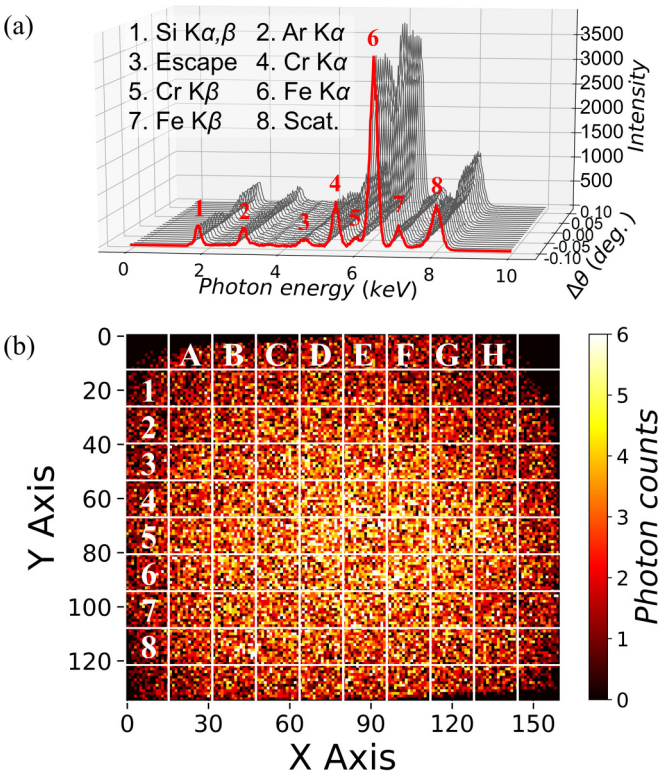

FIG. 3. Examples of the XSW imaging experiment data. (a) Full-field XRF spectra measured over the entire probing area. (b) An XRF image of Fe Kα taken at $\Delta\theta = +0.02^\circ$.

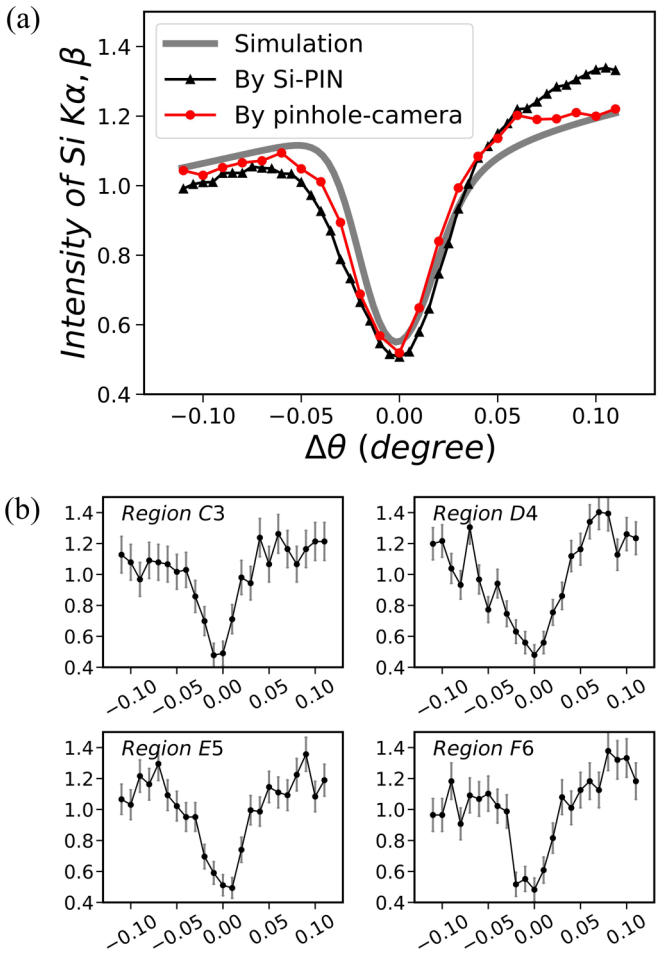

FIG. 4. XRF intensity profile of Si Kα, β from the silicon substrate. (a) Full-field profiles of the entire probing area, measured by either the Si-PIN detector or the pinhole camera. The experimental profiles match well with the simulated profile the vertical contrast of which has been reduced by half. (b) Microregion profiles of C3, D4, E5, and F6, respectively. All of these microregions are along the diagonal of the image.

were completely absorbed in air. Clearly the full-field XRF spectra are quite sensitive to the glancing angle θ when θ is scanned around θ_B. This is due to the motion of the XSW field in the sample. As the main focus of this paper is the iron impurity, one XRF image of Fe Kα was generated at each angle. For instance, the Fe Kα image taken at $\Delta\theta = +0.02^\circ$ is shown in Fig. 3(b). In this image, the central part is brighter than the peripheral parts because the image was measured by the pinhole camera, and the solid angle included in the measurement was larger for the center than for the periphery. Meanwhile, there is no clear pattern in the image, indicating that the iron impurity is dispersed randomly. In order to study the in-plane inhomogeneity, the entire image is equally divided into 100 microregions. The area of each microregion is 0.55×0.47 mm, which is obviously greater than the spatial resolution of the XRF imaging. Because the microregions at the outermost parts of the image may be partially sheltered by radiation-shielding material around the camera sensor, these microregions are abandoned and only the center 64 microregions are labeled and analyzed, as shown in Fig. 3(b).

D. Verifying the in-plane uniformity of the layer structure by XSW imaging

In this paper, the Ni/C PML sample is a well-established industrial product used to manufacture x-ray mirrors. Thus, it is reasonable to assume that its layer structure, which directly determines its performance as an x-ray mirror, has a perfect in-plane uniformity. It is assumed that its layer structure parameters for every microregion are always the same as those listed in Table I, which were determined by fitting the XRR pattern (Fig. 2) of the entire sample. This assumption provides much convenience for the subsequent XSW imaging analysis. However, for many unknown samples, the in-plane uniformity of the layer structure should be verified in advance. Generally, this requires the emerging technique of XRR imaging [24], which can independently measure the XRR patterns of every microregion in the sample. In this paper, the verification was verified by the XSW imaging experiment data.

To do this, we investigated the Si Kα, β intensity profile with respect to the θ scan. The Si Kα, β fluorescence comes from the silicon substrate of the sample. Its intensity is roughly proportional to the x-ray intensity at the surface of the substrate, which can be calculated using Parratt's recursive equations [22]. In the simulation, it was found that the intensity of Si Kα, β decreases greatly at θ_B [Fig. 4(a)], because the incident x rays are strongly reflected at the Bragg diffraction angle, and the x-ray intensity attenuates rapidly when the

x rays penetrate into the deeper bilayers. This effect, also known as the extinction effect, was clearly supported by the experimental result. In the full-field Si Kα, β intensity profile [Fig. 4(a)] that was measured over the entire probing area by either the pinhole-camera system or the Si-PIN detector, the dip at θ_B is quite clear. The two full-field profiles overlap with each other, even though the sizes of their corresponding probing areas are different. Meanwhile, the experimental profiles match well with the simulated profile, when vertical contrast has been reduced by half of the simulated profile. A possible reason for this contrast reduction might be that the bilayer thickness D fluctuates throughout the 150 repetitions, which has partially weakened the extinction effect.

To examine the in-plane uniformity of the layer structure, the Si Kα, β intensity profiles of every microregion have been investigated. As an example, the profiles of four microregions on the diagonal of the image are displayed in Fig. 4(b). Even though the profiles suffer from a large amount of counting noise due to the weak Si Kα, β intensity in detection, it is still clear that all of them have a dip at θ_B, and the amplitudes of the dips are all similar to that in the full-field Si Kα, β intensity profile. These results confirm our assumption that the layer structure of the sample has a perfect in-plane uniformity.

In this step, inspecting the XRF intensity profile of the silicon substrate has at least two functions. First, it can screen the "broken" points where the layer structure has been destroyed, because at the broken points there is no strong x-ray reflection and no intensity dip can occur in the corresponding microregion intensity profile. Second, it can examine the in-plane variation of the bilayer thickness D, because the intensity dip occurs exactly at the Bragg diffraction angle θ_B, and θ_B is extremely sensitive to the bilayer thickness D. Although the present approach is not as complete as the XRR imaging technique for verifying the in-plane uniformity of the layer structure, still it is quite attractive because all the necessary data can be obtained in only one angle scan using a laboratory x-ray source.

In the XSW imaging experiment, it is also possible to probe the layer structure by measuring the XRF intensity profile of nickel, because nickel is the major element that forms the frame of the PML. In this paper, the XRF of nickel was not measured. The Ni Kα intensity profile does not help in discussing the relationship between the intensity variations and θ_B. As already discussed, in the Si Kα, β intensity profile, the intensity dip occurs exactly at θ_B. The use of Si Kα, β is more useful. Furthermore, when nickel is excited by the incident x-ray beam, the intensity of Ni Kα is so strong that it interferes with the measurement of the small Fe Kα peak at the foot of the huge Ni Kα peak.

In addition, the intensity profile of the x-ray Compton scattering [25–27] is also a potential tool for probing the layer structure of the sample. A detailed discussion and experimental results are provided in the Supplemental Material [23].

E. XRF intensity profiles of the iron impurity

To study the distribution of the iron impurity, the intensity profiles of Fe Kα are plotted for the entire probing area and every microregion. The full-field profiles of the entire probing area are shown in Fig. 5(a). They were measured

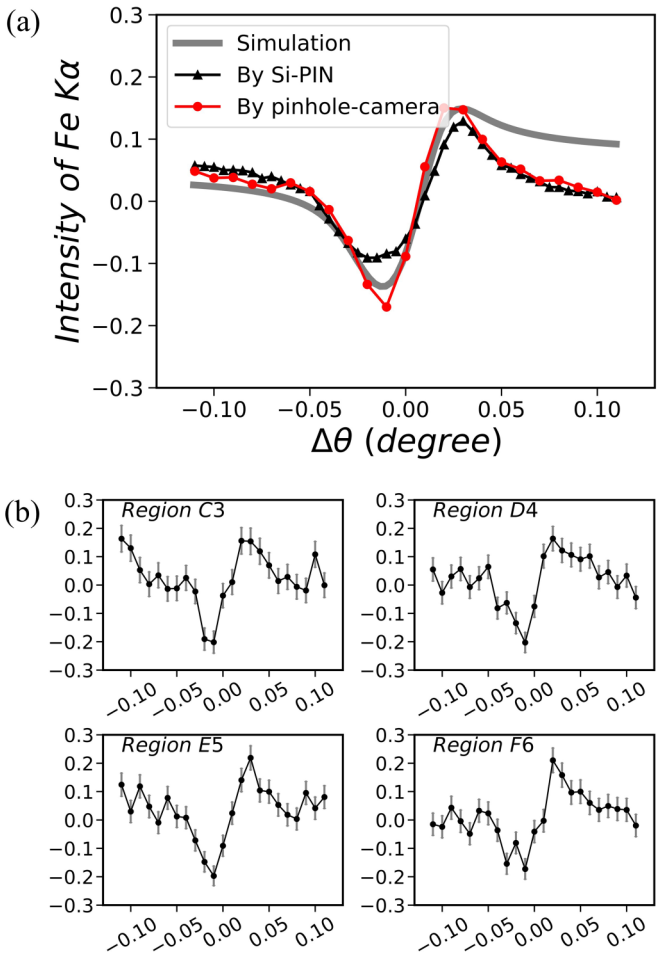

FIG. 5. XRF intensity profiles of Fe Kα from the iron impurity. (a) Full-field profiles of the entire probing area, measured by either the Si-PIN detector or the pinhole camera. The experimental profiles match well with the simulated profile when the depth of the iron impurity is assumed to be at the center of each nickel layer ($Z = 7$ Å) and the vertical contrast of the simulated profile has been reduced to 20%. (b) Microregion profiles of C3, D4, E5, and F6, respectively. All of these microregions are along the diagonal of the image.

by the pinhole camera and the Si-PIN detector, respectively. The profiles of all 64 microregions are displayed in the Supplemental Material [23]. As an example, in Fig. 5(b) the profiles of four microregions on the diagonal of the image are shown. It is noted that the two full-field intensity profiles are nearly overlapped with each other although the size of their corresponding probing area is different. This indicates that the average impurity depth distributions in the two probing areas are quite similar, and the two experimental schemes have an equivalent performance in estimating the average impurity depth distribution in a wide probing area. Moreover, the scheme of XSW imaging provides additional information independently in every microregion.

F. Analyzing large amounts of XSW imaging data by the feature map

To decode the experimental Fe Kα intensity profiles and reveal the distribution of the iron impurity, the experimental

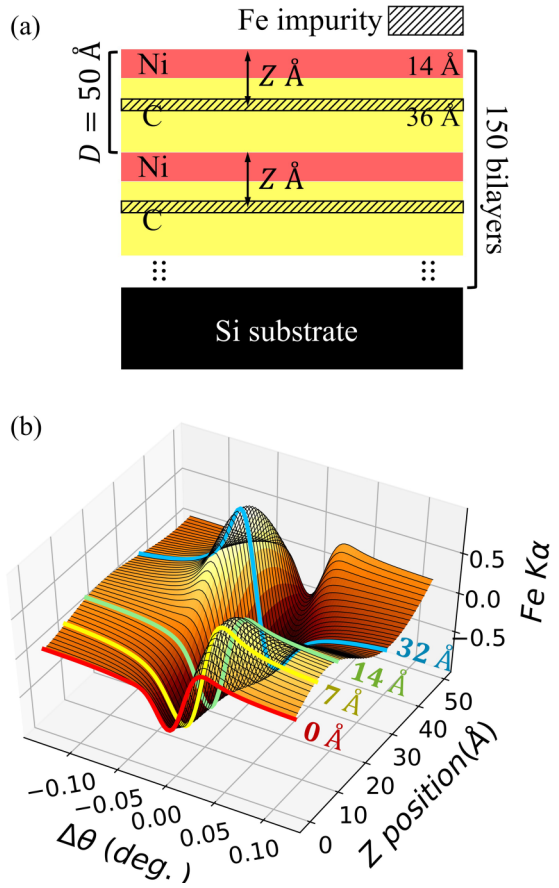

FIG. 6. Simulation of the iron impurity depth distribution and the corresponding Fe Kα intensity profile. (a) Model of the iron impurity depth distribution. (b) Simulated profiles. The shape of the profiles changes greatly as the depth Z of the iron impurity moves from 0 to 49 Å.

results have been compared with simulations. In this paper, we simulated the Fe Kα intensity profile by assuming a model of the impurity depth distribution. In the model [Fig. 6(a)], the iron impurity is dispersed in a thin slab at a depth of ZÅ in every Ni/C bilayer. Here, the reference plane is the top of every nickel layer and the downward direction is positive. The model of the impurity depth distribution correlates with Eq. (2). In the model, the coherent position z_A, which describes the "average" position of the impurity in the depth direction, equals Z. The coherent fraction f_A, which relates to the spreading width of the impurity in the depth direction, equals 1. Therefore, the present model is a good demonstration to show how the Fe Kα intensity profile is influenced by the average position of the iron impurity in the depth direction, even though the model does not enumerate all the possibilities of the impurity depth distribution.

While Eq. (2) provides the analytical expression to calculate the XRF intensity profile $Y(\theta)$ around the Bragg diffraction angle, in this simulation Parratt's recursive equations [22] were used to calculate the depth distribution of the electric-field strength $E(z)$, and then $Y(\theta)$ was simulated by

$$Y(\theta) = \int |E(\theta, z)|^2 \rho(z) dz \qquad (5)$$

where $\rho(z)$ denotes the impurity depth distribution. This recursive numerical method is widely adopted in much XSW research because it can calculate the XRF intensity profile in any angle region. In Eq. (5), the absorption of Fe Kα in the sample is omitted because the Ni/C layers are so thin that the absorption is rather weak. All the simulated Fe Kα intensity profiles corresponding to Z from 0 to 49 Å are shown in Fig. 6(b).

In Fig. 6, the vertical contrast of the simulated profiles is larger than that of the experimental results. There are two reasons for this. First, in the simulation model, it is assumed that the iron impurity is dispersed in a thin slab and the corresponding coherent fraction f_A equals 1. However, the actual iron impurity may have a spreading width in the depth direction, and in this case f_A becomes smaller than 1. This will reduce the amplitude of the cosine function and subsequently the vertical contrast of the XRF intensity profile. Second, in the actual Ni/C PML sample, the bilayer thickness D may have some variation throughout the 150 repetitions. This will reduce the intensity contrast between the XSW nodal planes and antinodal planes; consequently, the vertical contrast of the XRF intensity profile will be also reduced.

In the estimation for the entire probing area, it has been found that the two full-field XRF intensity profiles have the best match with the simulated profile when the depth of the iron impurity is assumed to be at the center of every nickel layer ($Z = 7$ Å), and the vertical contrast is assumed as 20% of the simulated profile [Fig. 5(a)]. However, in the XSW imaging analysis, an unmanageably large number of microregion profiles were obtained. It became too cumbersome and labor intensive to find the best match for every microregion profile. For this reason, a method of feature mapping has been proposed for comparing XRF intensity profiles. In this method, each intensity profile is converted to a feature vector (S_1, S_2, S_3) that describes the shape of the profile but neglects its vertical contrast. Thus, the comparison of many profiles can be simultaneously visualized by plotting their corresponding feature vectors in a feature map.

In XSW analysis, researchers mainly care about the angle region around the Bragg diffraction angle where a strong XSW field forms. In this paper, the width of the Bragg region is defined as the width of the Bragg diffraction peak in the XRR pattern, which is $\pm 0.045^\circ$ with respect to θ_B. On the other hand, based on Eq. (2), the XRF intensity profile around the Bragg diffraction angle is a distortion of half a period of a cosine function. Thus, the most important feature of one XRF intensity profile is its two extreme points in the Bragg region: the crest and the trough. For this reason, the feature vector should be strongly influenced by the two extreme points. The detailed procedure for generating the feature vector is as follows. Firstl, an intensity profile is normalized by its average intensity in the Bragg region; subsequently, the average intensity is taken as the baseline. Second, the Bragg region is divided into three parts by the two extreme points. Third, for the three parts, the three variables in the feature vector (S_1, S_2, S_3) describe the size of the area enclosed by the profile and the baseline, respectively. The area above the baseline is taken as positive and the area below the baseline is negative. In the final step, the three variables are normalized by the size of the absolute area of the entire Bragg region. The expressions

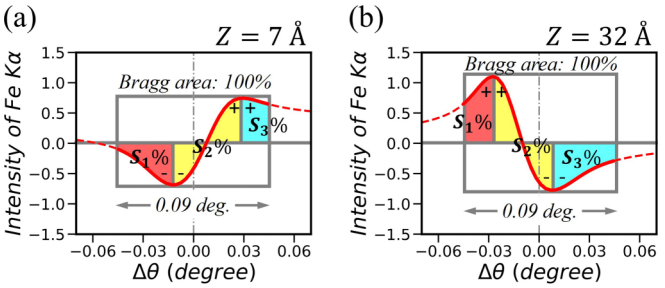

FIG. 7. Illustration of how to convert an XRF intensity profile into a feature vector. (a) The simulated profile corresponds to the model in which the depth of the iron impurity is at the center of every nickel layer ($Z = 7$ Å). In this case, $S_1 < 0$ and $S_3 > 0$. (b) The simulated profile corresponds to the model in which the depth of the impurity is at the center of every carbon layer ($Z = 32$ Å). In this case, $S_1 > 0$ and $S_3 < 0$.

are given by

$$S_1 = \frac{\int_{\theta_B-0.045^\circ}^{\theta_1} Y(\theta)d\theta}{S},$$
$$S_2 = \frac{\int_{\theta_1}^{\theta_2} Y(\theta)d\theta}{S}, \quad (6)$$
$$S_3 = \frac{\int_{\theta_2}^{\theta_B+0.045^\circ} Y(\theta)d\theta}{S},$$

where θ_1 and θ_2 denote the first and the second extreme points, respectively. The dominator S denotes the absolute area size of the entire Bragg region, given by

$$S = \int_{\theta_B-0.045^\circ}^{\theta_B+0.045^\circ} |Y(\theta_2) - Y(\theta_1)|d\theta. \quad (7)$$

Two examples of calculating the feature vector are given in Fig. 7. Since the sum of the three variables is zero, the terminating position of a feature vector (S_1, S_2, S_3) can be plotted in a ternary feature map. Figure 8(a) shows a feature map that has the feature points corresponding to all the simulated intensity profiles. It is noted that the feature point moves in the map while the depth distribution of the iron impurity moves from $Z = 0$ to 49 Å. In detail, when the iron impurity is in the nickel layers, the corresponding feature points are gathered in the left side of the map; when the impurity is in the carbon layers, the corresponding feature points are in the right side; and when the iron impurity is at the graded interfaces between the nickel layers and carbon layers, the corresponding feature points are mostly dispersed in the center of the map. Based on this feature map, it is found that the XSW analysis has a quite nice depth resolution and it is very sensitive to the interfaces in the nanolayer structure.

A feature map that presents the result of the full-field XSW analysis is shown in Fig. 8(b). The two feature points represent the measurement result of the pinhole camera and the Si-PIN detector, respectively. They are quite close to each other. This agrees with the fact that the two corresponding profiles are nearly overlapped in Fig. 5(a), indicating again that the two experimental schemes have equivalent performance in estimating the average impurity depth distribution in a wide

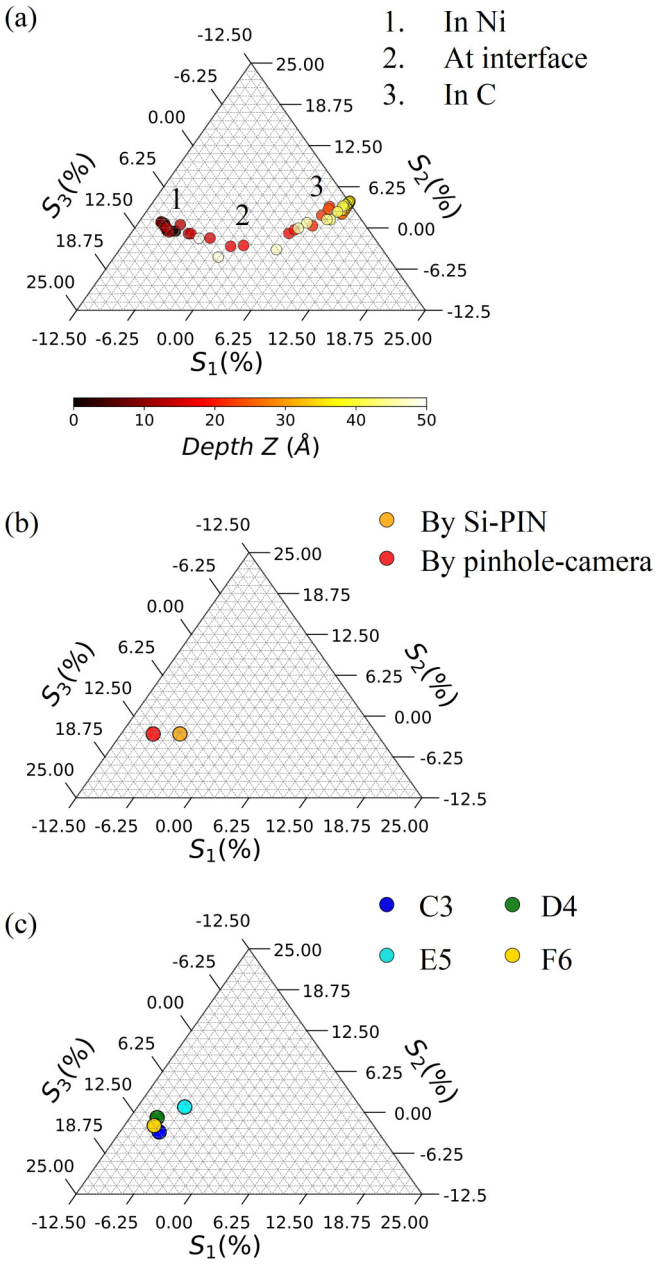

FIG. 8. Feature map for Fe Kα intensity profiles. (a) The feature points corresponding to all the simulated profiles. In the simulation model, the center of the iron impurity in the depth direction moves from $Z = 0$ to 49 Å. (b) The two feature points corresponding to the full-field intensity profiles of the entire probing area, measured by the pinhole camera and the Si-PIN detector, respectively. (c) The four feature points corresponding to the microregion profiles of C3, D4, E5, and F6, respectively.

probing area. Meanwhile, the two experimental feature points are in the same region corresponding to the simulation model in which the iron impurity is in the nickel layers. This agrees with the fact that the experimental profiles nearly overlap with the simulated profile of $Z = 7$ Å.

A feature map that shows the result of all 64 microregion profiles is displayed in the Supplemental Material [23]. Here, as an example, the feature points corresponding to four

microregions are shown in Fig. 8(c). It must be noted that, although the microregion feature points have some dispersion, they are clearly clustered in one small area of the map that corresponds to the nickel layer. In other words, none of the microregion feature points are grouped in the region corresponding to the carbon layer or the graded interface. Consequently, it is concluded that the iron impurity in the Ni/C PML sample is always correlated with the nickel layers, and the center of the iron depth distribution never enters into the carbon layers for any microregion in the entire probing area. For this reason, it can be inferred that the iron impurity originated as a contaminant in the source material that was used to deposit the nickel layers.

In this paper, using the feature map is a very efficient way to process the large number of microregion profiles and show their relationships. Furthermore, the influence of the counting noise can be directly visualized by using the feature map. On the feature map, the position of one feature point may vibrate because of the counting noise in its corresponding XRF intensity profile. The vibration radius is proportional to the level of counting noise. In this experiment, the experimental microregion profiles suffer from a high level of counting noise due to the weak x-ray intensity. For this reason, it is not always straightforward to use least-square fitting to find the best match between each experimental profile and the corresponding simulated profile. However, after plotting all the microregion feature points on the feature map, the distribution of the impurity in the sample becomes apparent because it is possible to appreciate the dispersion and grouping of all the feature points simultaneously.

G. Discussion

In this paper, an in-plane imaging capability was added to the conventional XSW technique. The XSW imaging technique developed here has a level of performance equivalent to the conventional XSW technique in the full-field analysis of a wide probing area. In addition, the XSW imaging technique provides independent information on every microregion. Although the XSW imaging technique was mostly developed for studying nonuniform samples, in this paper it is also indispensable for verifying the uniformity of the Ni/C PML sample. Using the conventional XSW technique, one can only obtain a simple estimation of the average iron impurity located in the Ni layers, but the sample can still be nonuniform and the depth distribution of the impurity may have many variations in different microregions. Only by using the XSW imaging technique can the depth distribution of the impurity in all microregions be resolved and the in-plane uniformity of the sample be affirmed.

In this paper, the in-plane spatial resolution is around 160 μm, which is mainly limited by the diameter of the pinhole. A smaller pinhole can optimize the imaging resolution, but it decreases the detected XRF intensity. At the present stage, this spatial resolution is a compromise necessitated by the x-ray intensity during the measurement. Based on our previous study, when the incident x-ray intensity is strong enough, the spatial resolution could be optimized to $\sim$15 μm by reducing the pinhole diameter [19] or by replacing the pinhole aperture with a thin collimator plate [13]. Clearly this in-plane spatial resolution is much worse than the atomic-scale depth resolution of the XSW analysis. However, many actual nanolayer structures may have a quite large area size of several square centimeters to square millimeters despite their nanoscale thickness. Consequently, the nanolayers may have macroscopic defects, patterns, and in-plane inhomogeneity that could have been introduced during the preparation process. In this case, an in-plane spatial resolution at the submillimeter level to micron level is very useful.

There is also another technique called XSW imaging [28,29]. The technique applies to a single crystal. It performs the XSW measurements twice by successively choosing two different sets of crystal planes as the reflection plane. This powerful technique is able to sketch a three-dimensional map of the foreign atoms at a crystal surface, and its spatial resolution in all directions is atomic scale. However, the technique also requires uniformity of the sample throughout the entire probing area so that the technique is obviously quite different from the one employed in this paper.

In the experiment, the major problem is the x-ray intensity. The iron impurity in the Ni/C PML sample is only present in very small amounts; hence, its XRF intensity is not strong. The energy-dispersive XRF imager was constructed by modifying a visible-light CMOS camera; consequently, its detection efficiency for x rays is not high. The utilization of the micropinhole also sacrifices a considerable amount of the XRF intensity. For all these reasons, the detected XRF intensity was not high enough, even though the XRF imaging experiment lasted for several days. As a result, the counting noise in the microregion XRF intensity profiles is a serious limitation. Nevertheless, this problem could be easily solved by increasing the intensity of the incident x-ray beam. In this paper, the experiment was carried out with using a laboratory x-ray tube on account of its stability during the long-term measurements. However, moving the experiment to a brilliant synchrotron radiation source seems to be attractive, not only because of the high intensity but also for the perfect beam collimation.

For more than 50 years, the XSW technique has been a powerful tool for characterizing a wide variety of nanolayers, surfaces, and interfaces [30]. In recent years, the technique has also shown its potential for investigating many new materials such as multilayer electrodes [31–34] and so on. In principle, the proposed XSW imaging technique can be easily adopted to all the material systems where the conventional XSW technique works. Since the XSW imaging technique can reveal the depth distribution of the elements in every microregion, it offers a systematic description of the impurity distribution. Thus, the relation between the impurity distribution and the performance of the sample may become clearer. In the meantime, since the XSW imaging technique does not require a uniform sample and allows the sample to have some macroscopic patterns and defects, the scope of application of XSW analysis will certainly be widened. For instance, the XSW imaging technique would make it possible to locate the contaminants, defects, and layer distortions in Langmuir-Blodgett films [35]. Also, it would be possible to visualize the cracks or the element segregation at the buried interface when a multilayer material is fatigued.

IV. CONCLUSIONS

In the present paper, a technique—XSW imaging—has been proposed that combines conventional XSW analysis with an in-plane imaging capability. The XSW imaging technique aims to visualize the in-plane variation of the impurity depth distribution in nanolayer structures. The technique has been successfully applied to study the distribution of the iron impurity in a nickel/carbon periodic multilayer sample. Moreover, a method of feature mapping has been proposed to process the large amounts of XRF imaging data efficiently. The technique is very promising for the analysis of many planar material systems as well as the visualization of the element patterns at buried interfaces.

ACKNOWLEDGMENTS

The present paper is a part of W.Z.'s Ph.D. research at Tsukuba University under the supervision of K.S. This work was partly supported by JSPS KAKENHI Grant No. JP18J12732.

[1] J. Zegenhagen and A. Kazimirov, *The X-Ray Standing Wave Technique: Principles and Applications* (World Scientific, Singapore, 2013).
[2] B. W. Batterman, Phys. Rev. **133**, A759 (1964).
[3] B. W. Batterman, Phys. Rev. Lett. **22**, 703 (1969).
[4] P. L. Cowan, J. A. Golovchenko, and M. F. Robbins, Phys. Rev. Lett. **44**, 1680 (1980).
[5] J. A. Golovchenko, J. R. Patel, D. R. Kaplan, P. L. Cowan, and M. J. Bedzyk, Phys. Rev. Lett. **49**, 560 (1982).
[6] T. W. Barbee and W. K. Warburton, Mater. Lett. **3**, 17 (1984).
[7] D. K. G. de Boer, Phys. Rev. B **44**, 498 (1991).
[8] M. Bedzyk, D. Bilderback, G. Bommarito, M. Caffrey, and J. Schildkraut, Science **241**, 1788 (1988).
[9] M. J. Bedzyk, G. M. Bommarito, and J. S. Schildkraut, Phys. Rev. Lett. **62**, 1376 (1989).
[10] M. Bedzyk, G. Bommarito, M. Caffrey, and T. Penner, Science **248**, 52 (1990).
[11] P. Fenter, L. Cheng, S. Rihs, M. MacHesky, M. J. Bedzyk, and N. C. Sturchio, J. Colloid Interface Sci. **225**, 154 (2000).
[12] J. M. Bloch, M. Sansone, F. Rondelez, D. G. Peiffer, P. Pincus, M. W. Kim, and P. M. Eisenberger, Phys. Rev. Lett. **54**, 1039 (1985).
[13] K. Sakurai and H. Eba, Anal. Chem. **75**, 355 (2003).
[14] O. Scharf, S. Ihle, I. Ordavo, V. Arkadiev, A. Bjeoumikhov, S. Bjeoumikhova, G. Buzanich, R. Gubzhokov, A. Günther, R. Hartmann, M. Kühbacher, M. Lang, N. Langhoff, A. Liebel, M. Radtke, U. Reinholz, H. Riesemeier, H. Soltau, L. Strüder, A. F. Thünemann, and R. Wedell, Anal. Chem. **83**, 2532 (2011).
[15] F. P. Romano, C. Caliri, L. Cosentino, S. Gammino, L. Giuntini, D. Mascali, L. Neri, L. Pappalardo, F. Rizzo, F. Taccetti, U. Catania, and V. A. Doria, Anal. Chem. **86**, 10892 (2014).
[16] W. Zhao and K. Sakurai, Rev. Sci. Instrum. **88**, 063703 (2017).
[17] W. Zhao and K. Sakurai, ACS Omega **2**, 4363 (2017).
[18] W. Zhao and K. Sakurai, Sci. Rep. **7**, 45472 (2017).
[19] W. Zhao and K. Sakurai, J. Synchrotron Rad. **26**, 230 (2019).
[20] N. Hertel, G. Materlik, and J. Zegenhagen, Z. Phys. B **58**, 199 (1985).
[21] J. Zegenhagen, Surf. Sci. Rep. **18**, 202 (1993).
[22] L. G. Parratt, Phys. Rev. **95**, 359 (1954).
[23] See Supplemental Material at http://link.aps.org/supplemental/10.1103/PhysRevMaterials.3.023802 for additional information.
[24] J. Jiang, K. Hirano, and K. Sakurai, J. Appl. Crystallogr. **50**, 712 (2017).
[25] S. Annaka, S. Kikuta, and K. Kohra, J. Phys. Soc. Japan **21**, 1559 (1966).
[26] W. Schulke, U. Bonse, and S. Mourikis, Phys. Rev. Lett. **47**, 1209 (1981).
[27] J. A. Golovchenko, D. R. Kaplan, B. Kincaid, R. Levesque, A. Meixner, M. F. Robbins, and J. Felsteiner, Phys. Rev. Lett. **46**, 1454 (1981).
[28] J. S. Okasinski, C. Y. Kim, D. A. Walko, and M. J. Bedzyk, Phys. Rev. B **69**, 041401 (2004).
[29] A. A. Escuadro, D. M. Goodner, J. S. Okasinski, and M. J. Bedzyk, Phys. Rev. B **70**, 235416 (2004).
[30] E. Schneck and B. Demé, Curr. Opin. Colloid Interface Sci. **20**, 244 (2015).
[31] T. T. Fister, J. Esbenshade, X. Chen, B. R. Long, B. Shi, C. M. Schlepütz, A. A. Gewirth, M. J. Bedzyk, and P. Fenter, Adv. Energy Mater. **4**, 1301494 (2014).
[32] G. Evmenenko, T. T. Fister, D. B. Buchholz, Q. Li, K. Chen, J. Wu, V. P. Dravid, M. C. Hersam, P. Fenter, and M. J. Bedzyk, ACS Appl. Mater. Interfaces **8**, 19979 (2016).
[33] X. Chen, T. T. Fister, J. Esbenshade, B. Shi, X. Hu, J. Wu, A. A. Gewirth, M. J. Bedzyk, and P. Fenter, ACS Appl. Mater. Interfaces **9**, 8169 (2017).
[34] G. Evmenenko, T. T. Fister, D. B. Buchholz, F. C. Castro, Q. Li, J. Wu, V. P. Dravid, P. Fenter, and M. J. Bedzyk, Phys. Chem. Chem. Phys. **19**, 20029 (2017).
[35] J. A. Zasadzinski, R. Viswanathan, L. Madsen, J. Garnae, and D. K. Schwartz, Science **263**, 1726 (1994).